Catalysis Today 157 (2010) 131–136

Contents lists available at ScienceDirect

Catalysis Today

journal homepage: www.elsevier.com/locate/cattod

Simple approach to prepare mesoporous silica supported mixed-oxide nanoparticles by *in situ* autocombustion procedure

D. Sellam[a,b], M. Bonne[a], S. Arrii-Clacens[a], G. Lafaye[a], N. Bion[a], S. Tezkratt[b], S. Royer[a,*], P. Marécot[a], D. Duprez[a]

[a] *Université de Poitiers, LACCO UMR 6503 CNRS, 40 avenue du recteur Pineau, 86022 Poitiers, France*
[b] *LCAGC, Hasnaoua 1, Université Mouloud Mammeri, Tizi Ouzou 15000, Algeria*

ARTICLE INFO

Article history:
Available online 14 April 2010

Keywords:
Autocombustion
Perovskite
Mesoporous
Nanoparticles
Oxygen mobility

ABSTRACT

$LaCoO_3$-based nanocomposites were prepared by an *in situ* autocombustion procedure of a glycine–nitrate complex in mesoporous silica supports. For this purpose, two silica supports with different pore sizes (3.0 nm for the HMS-type silica; 8.2 nm for the SBA15-type silica) were prepared. The final materials were characterized using XRD, TEM, N_2-sorption and reactivities evaluated using oxygen isotopic exchange (OIE). One interesting point is the limited pore plugging, due to the low particle size obtained, when synthesis is specifically performed in large pore silica support (SBA15), as suggested by the limited pore volume decrease with respect to the HMS-based system. TEM coupled with EDXS analyses suggest the formation of crystalline mixed-oxide nanoparticles which have been observed with a cobalt to lanthanum ratio always close to 1. These nanoparticles exhibit high oxygen exchange capacity (1.2–2.3 times higher exchange capacities after 60 min of reaction), albeit a lower initial rate of exchange compared to the bulk reference sample (due to residual carbonate exchange). At the light of these results, it has been concluded that this method is efficient for producing nanocrystalline particles dispersed in silica pore structure.

1. Introduction

During the past 40 years, a growing attention from the catalysis community has been paid on perovskite-type mixed-oxides, of general formula ABO_3. Indeed, the pioneer works from Libby [1] and Voorhoeve et al. [2,3] evidenced a high activity of perovskites in oxidation reaction. In some rare cases, perovskites were found to exhibit catalytic activities comparable to noble-metal based catalysts [4]. Hence, these purely oxidic solids were logically proposed as potential candidates for the substitution of expensive and non thermally stable noble-metal oxidation catalysts [5], and were successfully introduced in three-way catalyst formulation by Dahaïtsu Motors [6]. Among the wide range of compositions that can be achieved (perovskite structure can be achieved when the tolerance factor defined as a function of the component ionic radii lies between 0.75 and 1), only a few are reported to be active. According to the literature, systems with lanthanum in A position, and cobalt or manganese in B position, are the most studied perovskite systems in gas phase oxidation reactions [7–9]. Recently, many successful attempts to use perovskite in other redox heterogeneous catalytic reaction than oxidation [10–15] were reported. In parallel with this extensive use of mixed-oxides in heterogeneous catalysis, much more efficient synthesis procedures were developed in order to obtain nanocrystalline perovskites presenting higher surface areas. Best results were obtained using autocombustion [16,17], reactive grinding (or mechanosynthesis) [18,19], and more recently nanocasting [20,21]. Unfortunately, such procedures always lead to polycrystalline solids having crystal size ranging from 10 nm to 15 nm. One of the other alternative proposed in literature consists in stabilizing nanocrystals on a support, such as mesostructured silica [22–29]. In addition to the increase of surface area due to the limited size of the clusters, we can expect an additional increase in catalytic activity for redox reaction due to the increase in oxygen mobility as already observed on bulk perovskite [30]. Unfortunately, most of the studies reported the formation of perovskite nanocrystals close to the silica pore size thus leading to a significant pore clogging.

Herein, we present the results obtained from the synthesis and characterization of lanthanum cobalt based nanocomposites in silica supports of different porosity. Synthesis is performed using a novel procedure involving impregnation of a glycine complex, followed by a combustion step. Contrary to the conventional impregnation of a citrate gel [22,23], this method allows to obtain highly dispersed particles in a reduced porosity, without segregation of perovskite crystals on the periphery of the mesoporous support [27].

* Corresponding author. Tel.: +33 (0)5 49 45 34 79; fax: +33 (0)5 49 45 37 41.
E-mail address: sebastien.royer@univ-poitiers.fr (S. Royer).

0920-5861/$ – see front matter © 2010 Elsevier B.V. All rights reserved.
doi:10.1016/j.cattod.2010.03.008

2. Experimental

2.1. Synthesis of the mesoporous supports

2.1.1. Synthesis of the HMS support (HMS)

A pure siliceous HMS support is synthesized according to a previous published procedure [31]. Typically, 76 mL of water is added to a solution containing 7.21 g of dodecylamine within 66 mL of absolute ethanol under stirring. After 90 min of dissolution, 26.8 g of TEOS is slowly added to the solution. After ageing, the white solid was recovered by filtration and washing. The solid was then dried at 75 °C for 2 days before being calcined at 600 °C for 6 h (*HMS-c600*).

2.1.2. Synthesis of the SBA-15 support (SBA15)

The SBA15 sample is prepared according to the procedure described by Roggenbuck et al. [32]. To a solution containing 12 g of P123 triblock copolymer in 370 mL of water and 37 mL of concentrated HCl previously heated at 40 °C, 24 g of TEOS is slowly added under stirring. After 6 h of ageing at 40 °C, the milky solution is transferred in an autoclave for hydrothermal treatment at 140 °C during 24 h. The solid is then recovered by filtration and washing. Finally, the solid is dried at 80 °C for one day before being calcined at 600 °C for 4 h (*SBA15-c600*).

2.2. In situ synthesis of the mixed-oxides

Perovskite loading in the composite is fixed at 15 wt.% over HMS and 20 wt.% over SBA15, namely *15LaCo-HMS* and *20LaCo-SBA15* nanocomposites, respectively. Masses of precursors ($La(NO_3)_3{\cdot}6H_2O$ and $Co(NO_3)_2{\cdot}6H_2O$) are adjusted to give after calcination, the desired loading. Corresponding masses of nitrate precursors are dissolved in 20 mL of distilled water, and glycine is added as complexing agent (ratio $(NO_3)^-$/glycine = 1). After mixing of the solution with 1.0 g of support, water is slowly evaporated, and temperature increased up to 300 °C for glycine auto-ignition. Before characterization, solids are calcined at 600 °C (*15LaCo-HMS-c600*) or 620 °C (*20LaCo-SBA15-c620*) for 4 h. Bulk $LaCoO_3$ is prepared as a reference using similar self-combustion conditions ($(NO_3)^-$/glycine ratio = 1).

2.3. Physical characterization

TG–DSC experiment is performed at each step of the synthesis on 20LaCo-SBA15. Signal is recorded between 50 °C and 800 °C under air flowing (total flow rate = 100 mL min^{-1}, temperature increase ramp = 5 °C min^{-1}) on a TA SDT 2960 instrument.

Powder wide-angle and small-angle XRD patterns are collected on a Bruker AXS D5005 X-ray diffractometer, using a Cu Kα radiation (λ = 1.54184 Å) as X-ray source. For small-angle analysis, signal is recorded for 2θ comprised between 0.75° and 5° with a step of 0.01° (step time of 10 s). For wide-angle analysis, signal is recorded for 2θ comprised between 10° and 50° with a step of 0.05° (step time of 2 s).

Specific surface area, pore size distribution and pore volume are obtained from N_2-sorption experiments. A known mass of sample was first heat treated under vacuum at 250 °C. Isotherms are collected on a Micromeritics TRISTAR instrument. The specific surface area, S_{BET}, is calculated from the linear part of the BET plot. The mesopore size distribution is determined from the desorption branch using the Barrett–Joyner–Halenda (BJH) formula. Mesopore volume is determined on the isotherms at $P/P_0 = 0.97$. ΔV_p is the pore volume decrease per weight percent of perovskite in the composite, calculated using the following formula:

$$\Delta V_p = \frac{((V_{p(\text{support})} - V_{p(\text{composite})})/V_{p(\text{support})}) \times 100}{\text{wt.\% perovskite}}$$

The pore structure, as well as the mixed-oxide particle distribution inside the silica grain, is evaluated by TEM coupled with energy dispersive X-ray spectroscopy (EDXS). Micrographs are obtained on a JEOL 2100 instrument (operated at 200 kV with a LaB_6 source and equipped with a Gatan UltraScan camera). Cation homogeneity inside silica, and composition of the crystallized particles are evaluated by EDX spectroscopy. Analysis is repeated on several nanoparticles in order to rach a mean value of mixed-oxide composition.

2.4. Oxygen isotopic exchange reaction $^{18}O/^{16}O$

The oxygen isotopic exchange (OIE) technique is used to evaluate oxygen mobility in the mixed-oxide phase in these novel composites and in the reference bulk perovskite sample. Full description of the exchange test and data treatment can be found elsewhere [27,30], and is only summarized here. The exchange mechanism can be described by the following equation, even if different mechanisms are depicted: $^{18}O_g + {}^{16}O_s \rightarrow {}^{16}O_g + {}^{18}O_s$, where s and g refer to oxygen from the solid and from the gas phase, respectively. For the exchange experiment, an equivalent of 20 mg of perovksite is inserted in a microreactor. Then the sample is heated at its calcination temperature under O_2 (ramp = 10 °C min^{-1}, $Q_{O_2} = 20$ mL min^{-1}), cooled down at 450 °C under O_2 and maintained at the same temperature under dynamic vacuum. Pure $^{18}O_2$ at a pressure of about 56.0 mbar was introduced into the reactor. Partial pressure evolutions in $^{18}O_2$ (mass 36), $^{16}O_2$ (mass 32), and $^{16}O^{18}O$ (mass 34) are followed by mass spectrometry for an experiment time of 60 min. α_g^{60} is the fraction of ^{18}O in the gas phase at 60 min. N_{ex}^{60} corresponds to the number of oxygen atoms exchanged from the solid after 60 min.

3. Results and discussion

3.1. "In situ" formation of the mixed-oxide

As described in the experimental part, a classical autocombustion procedure (LaCo-Bulk) consists in a first step of nitrate precursor dissolution in water followed by complexation with a fuel such as glycine, urea or ammonium nitrate. After complexation, water is slowly evaporated at 100 °C until a viscous gel is obtained, then temperature is increased up to 300 °C for fuel autoignition, much less violent in the composites than for the bulk materials. An additional calcination step can be needed for residual carbon elimination (formed by incomplete glycine combustion). The TG–DSC curves obtained for the LaCo-SBA15 sample after each step of the synthesis are presented in Fig. 1a–c. As shown, after a drying step at 100 °C (Fig. 1a), two exothermal peaks occurred at 180 °C and 275 °C on the DSC curve that is ascribed to the combustion process. This later achieves at 300 °C, with no more exothermal process visible above this temperature. After autocombustion at 300 °C, we can observe that glycine combustion is incomplete, and a further decrease of 5 wt.% is observed at 275 °C (Fig. 1b). This weight loss is no more visible on the sample after further calcination at 620 °C, and residual weight loss is mainly attributed to water desorption (at low temperature, <200 °C) and to residual carbon combustion or support dehydration (at higher temperature than the calcination temperature, >620 °C). Overall, this clearly shows that the calcination step is necessary on the composites before their characterization or use as catalyst.

3.2. Pore structure in the nanocomposites

Small-angle X-ray diffraction patterns (supports and derived nanocomposites) are presented in Fig. 2. The HMS-c600 support

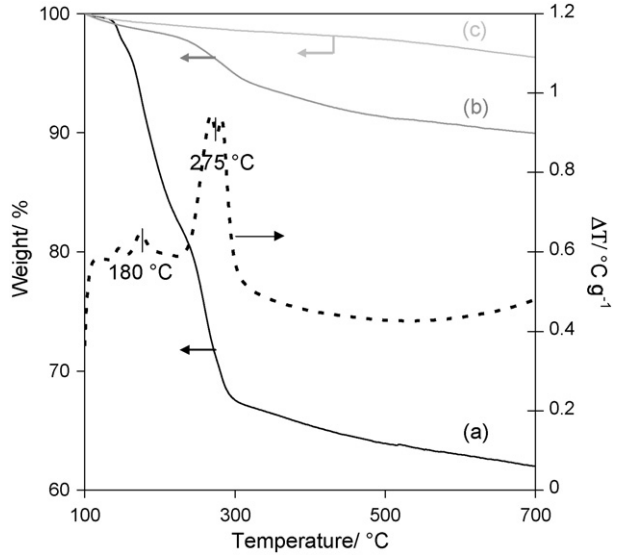

Fig. 1. TG–DSC curves obtained for LaCo-SBA15: (a) After drying at 100 °C (dotted line, DSC signal); (b) after autocombustion at 300 °C; (c) after calcination at 620 °C.

(dotted line, Fig. 2a) exhibits an intense and wide diffraction peak at $2\theta = 2.13°$, characteristic of the (1 0 0) crystallographic plane of the hexagonal structure for HMS solids. Autocombustion cycle on the nanocomposite (full line, Fig. 2a) results in a strong attenuation of the (1 0 0) reflection. Note that the maximum of the residual diffraction peak is located at $2\theta = 1.98°$, a value close to that of the parent support. This means, as already proposed [22,27], that the periodicity of the pore structure is altered by the mixed-oxide formation or that the support pore filling results in an attenuation of the diffraction peaks. The diffraction pattern obtained for the SBA15-c600 sample (dotted line, Fig. 2b) shows three clearly identified peaks at $2\theta = 0.99°$, 1.61° and 1.84°. These three reflections

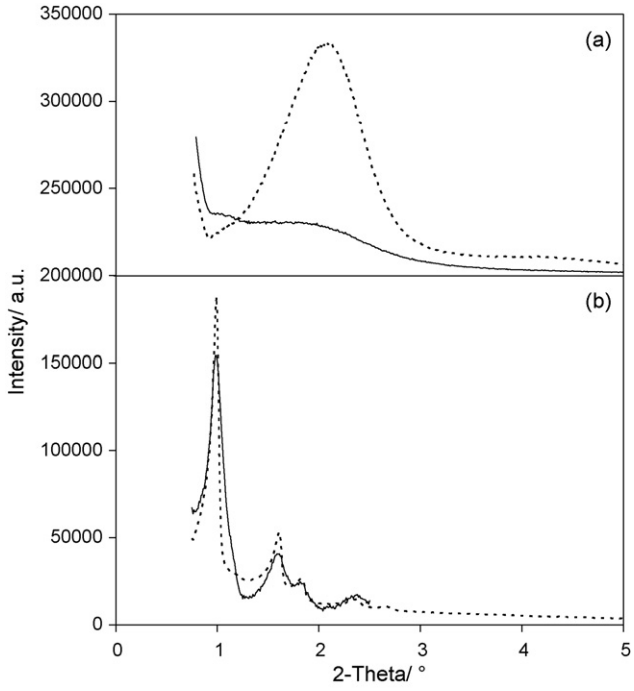

Fig. 2. Small-angle X-ray diffraction patterns obtained on (a) 15LaCo-HMS-c600 and (b) 20LaCo-SBA15-c620. Patterns obtained over the freshly calcined HMS and SBA supports (dotted line) are added for sake of comparison (HMS solids are offset from 200,000 counts).

are easily attributed to the (1 0 0), (1 1 0) and (2 0 0) reflections in the hexagonal structure. Similar diffraction pattern is obtained on 20LaCo-SBA15-c620, with three reflections located at exactly the same 2θ values. In this last case, it is evident that the autocombustion cycle, necessary for the mixed-oxide formation, has no impact on the pore structure of the support. In other words, the support porosity seems to be not affected by the autocombustion process.

3.3. Physical properties

Physical properties deduced from the N_2 adsorption–desorption isotherms are summarized in Table 1 and plotted in Fig. 3. HMS-c600 support presents a surface area higher than 800 $m^2\,g^{-1}$, limited pore size (3.0 nm), and large pore volume (1.00 $cm^3\,g^{-1}$). These results are in agreement with those obtained over solids synthesized using similar procedure with dodecylamine as structuring agent. A largely lower surface area is developed on SBA15-c600 support (only 545 $m^2\,g^{-1}$) while larger mean pore size and higher mesopore volume are also obtained. These differences are easily explained by the use of a different template (*i.e.* P123) leading to the formation of porous solids exhibiting wider inorganic wall and larger pore size, obviously leading to lower surface area. It is worth noting that values reported for this last support are also in agreement with those reported in the literature. Isotherms and corresponding BJH pore size distributions are presented in Fig. 3a and b. For the two calcined supports, type IV isotherms are obtained, according to the IUPAC classification. This kind of isotherm, characteristic of mesoporous solids, is characterized by an abrupt adsorption followed by a long adsorption plateau until $P/P_0 = 1$. Due to the sharp adsorption and desorption steps, narrow pore size distributions are obtained (Fig. 3b).

The autocombustion cycle for mixed-oxide formation leads to important modifications of the material physical properties (Table 1). Indeed, decreases in surface area and pore volume are observed, while mean pore size remains at a value close to that of the parent support (2.8 nm and 3.0 nm for the 15LaCo-HMS-c600 and HMS-c600, respectively, Fig. 3b). The decrease in pore volume normalized per percent of perovksite in the composite (ΔV_p, Table 1) is found to vary between 4.13 (for the HMS-derived composite) and 1.45 (for the SBA15-derived composite). As a result, the pore volume shrinkage is more pronounced over the HMS system, suggesting a more significant pore plugging phenomenon due to the mixed-oxide particles. It is important to note that surface areas reported on the composites are largely higher than on bulk perovskite (10 $m^2\,g^{-1}$, Table 1) due to the silica support contribution. While large differences in physical properties are obtained between the nanocomposites and the parent supports, isotherm shapes and long range ordering remain globally unchanged according to the type IV isotherms and small-angle X-ray diffraction patterns obtained for both materials (Fig. 3a), hence supporting, that the pore structure of the support is almost maintained in the nanocomposites.

The main difference between the two nanocomposites has been attributed to the different evolution of the pore volume. Then, larger pore size obtained on SBA15 allowed a lower decrease in pore volume per perovskite loading unit, suggesting that *in situ* autocombustion synthesis is more appropriate in large pore host material to limit pore plugging.

3.4. Structure of the mixed-oxide particles

Wide-angle X-ray diffraction patterns are presented in Fig. 4. LaCo-Bulk reference presents intense and sharp reflections characteristic of $LaCoO_3$ crystal structure (JCPDS file no. 09-0358). As a matter of fact, no reflection characteristic of the single oxides (Co_3O_4, La_2O_3) can be observed. This clearly indicates that the

Table 1
Physical properties of the calcined supports and derived $LaCoO_3$ nanocomposites.

Sample	Loading[a]/%	S_{BET}[b]/$m^2\ g^{-1}$	D_p[b]/nm	V_p[b]/$cm^3\ g^{-1}$	ΔV_p[c]/%$_{perov}^{-1}$	α_g^{60d}/%	N_{ex}^{60d}/at g^{-1}
LaCo-Bulk	–	10	–	–	–	80	21.1
HMS-c600	–	832	3.0	1.00	–	–	–
15LaCo-HMS-c600	14.2	585	2.8	0.38	4.13	68	48.9
SBA15-c600	–	545	8.2	1.26	–	–	–
20LaCo-SBA15-c620	20.9	410	7.9	0.89	1.45	77	24.8

[a] Perovksite loading as verified by ICP.
[b] S_{BET}, BET surface area; D_p, BJH mesopore size (desorption branch); V_p, mesopore volume.
[c] Pore volume decrease per weight percent of perovskite in the composite.
[d] α_g^{60}, fraction of ^{18}O atom in the gas phase; N_{ex}^{60}, number of oxygen atoms exchanged at 60 min per gram of perovskite.

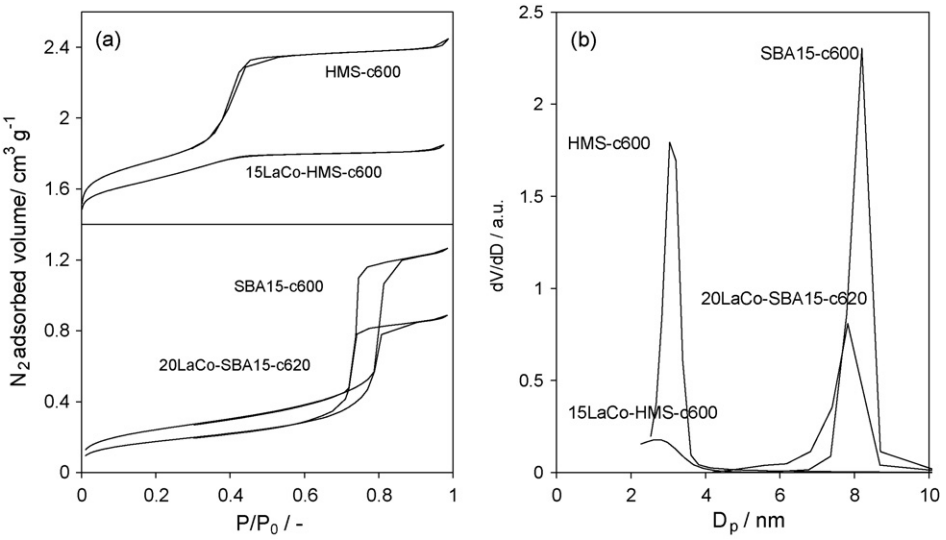

Fig. 3. N_2 adsorption–desorption curves (a) and corresponding BJH desorption pore size distribution (b) obtained over the nanocomposites (full line) and respective supports (dotted lines). Isotherms of HMS-based samples are shifted from a volume of 1.4 $cm^3\ g^{-1}$ for sake of clarity.

autocombustion procedure is efficient to produce perovskite with limited contamination by residual single oxides. Such narrow reflections are not visible on the two nanocomposite patterns. Indeed, only one broad and poorly defined diffraction peak at $2\theta = 33.2^\circ$, corresponding to the most intense reflection of the $LaCoO_3$ crystal structure, is observed on 15LaCo-HMS-c600 diffraction pattern. 20LaCo-SBA15-c620 pattern presents no reflection, except the baseline fluctuation related to the amorphous character of silica can be observed. This result could arise in different ways. First, the oxide precursors do not crystallize and remain amorphous. Alternatively, the formation of crystalline particles at a size below the detection limit of the XRD (~3–4 nm) can presumably occurred. The last reason can be the low content of perovskite in the composite (15 wt.% or 20 wt.%). However, this latter explanation could be ruled out since the hand mixing of 15 wt.% of bulk perovskite with the support allows an easy detection of the perovskite phase. Consequently, only an amorphous character or a low particle size is suggested to be responsible for the lack in diffraction in the 20–50° range.

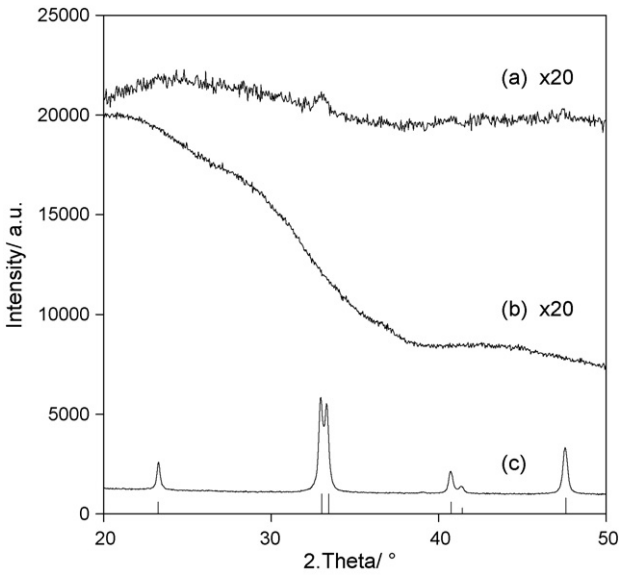

Fig. 4. X-ray diffraction patterns recorded on the 20–50° region for (a) 15LaCo-HMS-c600 and (b) 20LaCo-SBA15-c620, and (c) LaCo-Bulk.

3.5. Morphological properties of the composites

Results of TEM analysis for the SBA15 and derived nanocomposite are presented in Fig. 5. As illustrated, pure SBA15 support exhibits a well-defined hexagonal pore structure (Fig. 5a). Similar observation can be made on the low magnification TEM image of 20LaCo-SBA15-c620. Indeed, the hexagonal pore structure is still observed in Fig. 5b, even after mixed-oxide formation. This is consistent with XRD observations where diffraction peaks characteristic of the hexagonal pore structure were observed even after the autocombustion cycle (Fig. 2). The major difference with the parent support is the presence of darker zones located on the periphery of the ~8 nm pores. Focus on these darker zones allows to detect nanometric crystalline particles. It is interesting to note that most of the particles present a size lower than 5 nm and visi-

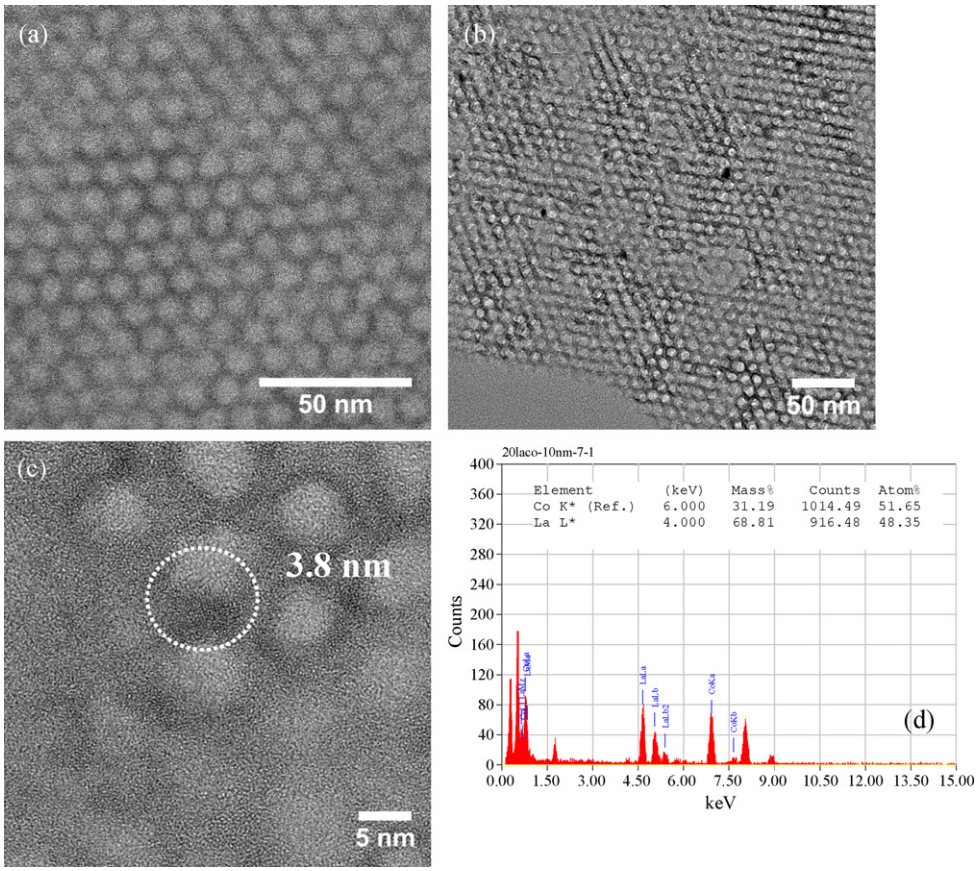

Fig. 5. Typical TEM micrograph obtained over (a) SBA15-c600 and (b) 20LaCo-SBA15-c620 samples. (c) Focus on a nanometric crystallized particle in 20LaCo-SBA15-c620; (d) corresponding 5 nm EDX spectroscopy obtained on a 4 nm isolated particle.

ble lattice fringes, as observed in Fig. 5c. Observation of Fig. 5b and c suggests that most of the pores remain open and limited size of the nanoparticles does not result in important pore plugging. Formation of larger particles cannot be excluded on the basis of TEM analysis, even if particles larger than 5 nm are not observed. Similar results were obtained over 15LaCo-HMS-c600, with the observation of small particles (<5 nm), dispersed in the silica micrometric grains (TEM images presented in Ref. [27]). Unfortunately, the formation of <5 nm particles in the small pores of the HMS support (D_p = 3.0 nm, Table 1) obviously leads to important pore plugging, as confirmed by the drastic decrease in pore volume on the nanocomposite derived from this support ($\Delta V_p = 4.13\%\%_{perov}^{-1}$, Table 1).

On the basis of the results obtained by TEM, the lack in diffraction peaks in the 20–50° region of the diffraction patterns is likely due to the limited size of the crystalline particles, more than the amorphous character of the particles. EDX spectroscopy on isolated nanometric particles is further performed to evaluate the cation homogeneity in these nanoparticles. A typical result, obtained using a 5 nm analysis zone, is presented in Fig. 5d. For the analyzed particle, a composition of 51.7 at.% of Co and 48.3 at.% of La is obtained. Analysis of 25 particles on different zones of the TEM grid always leads to atomic composition of 50.0 ± 7.0 at.%, suggesting a satisfying dispersion of the cations in the nanoparticles. Due to the punctual character of the EDXS analysis, the use of a global characterization technique is needed to assert the formation of the desired mixed-oxide structure all over the composite. Nevertheless, the crystalline character of the observed particles, in addition to the desired cation composition, suggests the formation of perovskite-type mixed-oxide nanoparticles dispersed in the silica porosity. It is important to note that the particle size does not depend on pore size of the host material as observed by electron microscopy.

3.6. Reactivity of the mixed-oxide nanoparticles

Reactivity of the nanoparticles was assessed by oxygen isotopic exchange (OIE) reaction. The evolution of the ^{18}O fraction in the gas phase with reaction time is presented in Fig. 6, and values of ^{18}O fraction in the gas phase and number of oxygen atoms from the solid

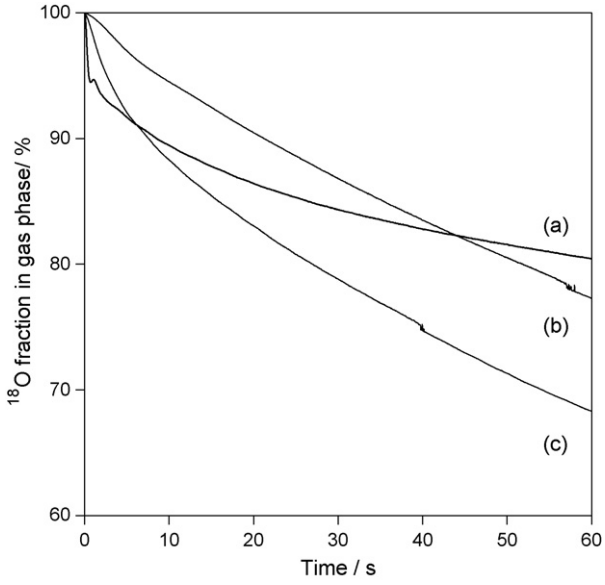

Fig. 6. Isotopic oxygen exchange curves recorded at T = 450 °C for (a) LaCo-Bulk, (b) 20LaCo-SBA15-c620 and (c) 15LaCo-HMS-c600.

exchanged at 60 min (N_{ex}^{60}) are summarized in Table 1. From Fig. 6, it is evident that initial exchange occurs more slowly over the two nanocomposites (curves b and c, Fig. 6) than on the bulk material (curve a). The fast exchange occurring during the first 3 min on the LaCo-Bulk sample was already attributed to the exchange of residual surface carbonates [27] (formed by reaction between accessible lanthanum and CO_2 from the atmosphere). Such exchange does not occurred over the two nanocomposites, and initial exchange occurs more slowly. At the end of the exchange experiment (60 min), lower ^{18}O fraction in gas phase is obtained for the two nanocomposites than for the LaCo-Bulk sample, showing striking improvement of exchange capacity (surface and bulk oxygen mobilities). Indeed, a 1.2 (20LaCo-SBA15-c620) to 2.3 (15LaCo-HMS-c600) times higher number of oxygen atoms exchanged (N_{ex}^{60} value, Table 1) is obtained over the nanocomposites with respect to the bulk material. Note that the highest exchange activity is obtained over the HMS-based nanocomposite, even if this solid presents a more important pore plugging phenomenon due to its low pore size. Unfortunately, it is not possible on the basis of the results presented here to conclude on the reason of this difference between the two nanocomposites, since mixed-oxide dispersion in silica seems similar for the two samples. We can only suggest, as already observed on bulk materials [30], that activity in oxygen exchange does not only depend on the accessible surface of the particles, but also on the bulk structure and defects in the nanoparticles.

While interesting oxygen exchange capacities are obtained, the nanocomposites do not present significant catalytic activity for methane oxidation reaction. For illustration, a methane conversion of 61% is obtained for LaCo-Bulk, only 17% is obtained with 20LaCo-SBA15-c620 at 600 °C in the reaction conditions reported Ref. [33] (flow (vol%): $1.0CH_4$–$4.0CO_2$–$4.0H_2O$–$18.2O_2$–$72.8N_2$, GHSV = 415,000 h^{-1}, total flow rate = 190 mL min^{-1}). Recent XANES and EXAFS results (not shown) suggest that the low valence state of cobalt (Co^{2+}) in the identified mixed-oxide structure is responsible for both the high oxygen transfer rates but also for the poor methane activation (requiring a redox $Co^{3+} \leftrightarrow Co^{2+}$ active site). Indeed, the high oxygen deficient solid, related to the measured valence of cobalt, could explain why high oxygen transfer rates are obtained on the samples if we consider that oxygen diffusion in the bulk proceeds though vacancies, why the low activities obtained for the nanocomposites can be explained by the reduced number of active redox sites in these solids. The reason of this low activity, as well as the mean to solve this problem, is actually under investigation, with the objective to determine the critical size of perovskite allowing a good balance between O_2 and CH_4 activation rates.

4. Conclusion

Two $LaCoO_3$-based nanocomposites were prepared according to an *in situ* autocombustion procedure in the porosity of mesoporous silica supports. HMS-type silica and a large pore SBA15-type silica were compared to evidence the effect of the pore size on the resulting mixed-oxide nanoparticle sizes. Subsequent characterization of the nanocomposites clearly shows that the synthesis procedure is efficient to obtain nanometric (<5 nm) crystallized particles. In addition, the SBA15-derived nanocomposite presents limited pore plugging, and can be described as supported nanoparticles dispersed in the porosity of the large pore silica. Multiple EDX spectroscopy analyses highlight a Co/La atomic ratio always close to 1 for the analyzed particles, which is in line with the perovskite stoechiometry. Compared to the bulk reference material, higher oxygen exchange capacities are obtained for the two composites, the highest exchange capacity being obtained for the HMS-derived nanocomposite. Despite the great reactivity of these solids, no significant catalytic performance has been observed for methane oxidation reaction, suggesting that different adsorption properties could occur for such nanometric particles with respect to the bulk LaCo reference.

Acknowledgments

The Algerian government is acknowledged for financial support (*D. Sellam*). The *Region Poitou-Charentes*, *France*, is acknowledged for the financial support through a Ph.D. Grant (*M. Bonne*). Authors want to thank *Julie Rousseau* from LACCO for TEM analysis.

References

[1] W.F. Libby, Science 171 (1971) 499.
[2] R.J.H. Voorhoeve, J.P. Remeika Jr., P.E. Freeland, B.T. Mathias, Science 177 (1972) 353.
[3] R.J.H. Voorhoeve, J.P. Remeika Jr., L.E. Trimble, Mater. Res. Bull. 9 (1974) 1393.
[4] H. Arai, T. Yamada, K. Eguchi, T. Seiyama, Appl. Catal. A 26 (1986) 265.
[5] S. Royer, C. Ayrault, C. Carnevillier, F. Epron, P. Marécot, D. Duprez, Catal. Today 117 (2006) 543.
[6] H. Tanaka, I. Tan, M. Uenishi, N. Kajita, M. Taniguchi, Y. Sato, K. Narita, N. Sato, Catalyst for clarifying exhaust gas, US Patent 7,205,257 (2005-12-01), to Cataler Co.
[7] G. Kremenic, J.M.L. Nieto, J.M.D. Tascon, L.G. Tejuca, J. Chem. Soc. Faraday Trans. 81 (1985) 939.
[8] T. Nitadori, T. Ichiki, M. Misono, Bull. Chem. Soc. Jpn. 61 (1988) 621.
[9] A. Baiker, P.E. Marti, P. Keusch, E. Fritsch, A. Reller, J. Catal. 146 (1994) 268.
[10] G. Sierra Gallego, C. Batiot-Dupeyrat, J. Barrault, E. Florez, F. Mondragón, Appl. Catal. A 334 (2008) 251.
[11] C. Guo, X. Zhang, J. Zhang, Y. Wang, J. Mol. Catal. A: Chem. 269 (2007) 254.
[12] R. Zhang, H. Alamdari, S. Kaliaguine, J. Catal. 242 (2006) 241.
[13] J.P. Dacquin, C. Dujardin, P. Granger, J. Catal. 253 (2008) 37.
[14] S. Royer, B. Levasseur, H. Alamdari, J. Barbier Jr., D. Duprez, S. Kaliaguine, Appl. Catal. B 80 (2008) 51.
[15] J.L. Sotelo, G. Ovejero, F. Martínez, J.A. Melero, A. Milieni, Appl. Catal. B 47 (2004) 281.
[16] L. Wachowski, S. Zielinscki, A. Burewicz, Acta Chim. Acad. Sci. Hung. 106 (1981) 217.
[17] D. Berger, C. Matei, F. Papa, G. Voicu, V. Fruth, Prog. Sol. State Chem. 35 (2007) 183.
[18] S. Kaliaguine, A. Van Neste, V. Szabo, J.E. Gallot, M. Bassir, R. Muzychuk, Appl. Catal. A 209 (2001) 39.
[19] S. Kaliaguine, V. Szabo, A. Van Neste, J.E. Gallot, M. Bassir, R. Muzychuk, J. Metastable Nanocrystalline Mater. 11 (2001) 39.
[20] Y. Wang, J. Ren, Y. Wang, F. Zhang, X. Liu, Y. Guo, G. Lu, J. Phys. Chem. C 112 (2008) 15293.
[21] H. Su, L. Jing, K. Shi, C. Yao, H. Fu, J. Nanoparticle Res. 12 (2010) 967.
[22] V.S. Nguyen, V. Szabo, D. Trong On, S. Kaliaguine, Micropor. Mesopor. Mater. 54 (2002) 51.
[23] N. Yi, Y. Cao, Y. Su, W.-L. Dai, H.-Y. He, K.-N. Fan, J. Catal. 230 (2005) 249.
[24] E.V. Makshina, S.V. Sirotin, V.V. Yushchenko, G.N. Mazo, M.W.E. van den Berg, K.V. Klementiev, W. Grunert, B.V. Romanovskii, Kinet. Catal. 47 (2006) 49.
[25] E.V. Makshina, S.V. Sirotin, M.W.E. van den Berg, K.V. Klementiev, V.V. Yushchenko, G.N. Mazo, W. Grunert, B.V. Romanovsky, Appl. Catal. A 312 (2006) 56.
[26] E.V. Makshina, N.S. Nesterenko, S. Siffert, E.A. Zhilinskaya, A. Aboukais, B.V. Romanovsky, Catal. Today 131 (2008) 427.
[27] M. Bonne, N. Bion, F. Pailloux, S. Valange, S. Royer, J.-M. Tatibouet, D. Duprez, Chem. Commun. (2008) 4504.
[28] J. Deng, L. Zhang, H. Dai, C.-T. Au, Appl. Catal. A 352 (2009) 43.
[29] I. Rivas, J. Alvarez, E. Pietri, M.J. Perez-Zurita, M.R. Goldwasser, Catal. Today 149 (2010) 388.
[30] S. Royer, D. Duprez, S. Kaliaguine, J. Catal. 234 (2005) 364.
[31] D.J. Macquarrie, D.B. Jackson, J.E.G. Mdoe, H.J. Clark, New J. Chem. 23 (1999) 539.
[32] J. Roggenbuck, G. Koch, M. Tiemann, Chem. Mater. 19 (2006) 4151.
[33] A. Baylet, S. Royer, C. Labrugère, H. Valencia, P. Marécot, J.M. Tatibouët, D. Duprez, Phys. Chem. Chem. Phys. 10 (2008) 5983.